

Simulation of High Reynolds Number Vascular Flows

Paul F. Fischer,^a Francis Loth,^b Seung E. Lee,^c Sang-Wook Lee,^d David S. Smith,^b and Hisham S. Bassiouny^e

^aMathematics and Computer Science Division, Argonne National Laboratory
Argonne, IL 60439, U.S.A.

^bDept. of Mechanical Engineering, University of Illinois,
Chicago, IL 60607, U.S.A.

^cDept. of Mechanical Engineering, Massachusetts Institute of Technology,
Cambridge, MA

^dImaging Research Laboratories, Robarts Research Institute,
London, ON N6A 5K8, Canada

^eSection of Vascular Surgery, University of Chicago,
Chicago, IL 60607, U.S.A.

1. Introduction

While much of the hemodynamics in a healthy human body has low Reynolds number, resulting in laminar flow, relatively high Reynolds number flow is observed at some specific locations, which can cause transition to turbulence. (The term “turbulence” refers to the motion of a fluid having local velocities and pressures that fluctuate randomly.) For example, the peak Reynolds number in the human aorta has been measured to be approximately 4000 [25]. Surgical constructions such as the arteriovenous (AV) graft, which consists of a prosthetic graft material surgically attached between an artery and a vein, also results in relatively high Reynolds number flow (1000–3000) [8,40]. Complex geometries such as a severe stenosis also can cause turbulent flow in the vasculature [22].

The simulation of turbulent vascular flows presents significant numerical challenges. Because such flows are only weakly turbulent, they lack an inertial subrange that is amenable to subgrid-scale modeling required for large-eddy or Reynolds-averaged Navier-Stokes simulations. The only reliable simulation approach at present is to directly resolve all scales of motion. While the Reynolds number is not high ($Re=1000-2000$, typ.), the physical dissipation is nonetheless small, and high-order methods are essential for efficiency. Moreover, turbulent blood flow exhibits a much broader range of scales than does its laminar (healthy) counterpart and thus requires an order of magnitude increase in spatial and temporal resolution. For example, recent work by Sherwin and Blackburn has shown that roughly one to two million gridpoints are required for spectral/spectral-element-based simulations of turbulence in an idealized stenosis [42].

In this paper, we discuss temporal and spatial resolution requirements for direct numerical simulation in two cases where turbulence is commonly found in the vasculature, namely, in a stenosed carotid artery and in the venous anastomosis of an arteriovenous graft. We also describe recent developments in the spectral element method designed specifically for the simulation of high-Reynolds number vascular flows. The paper is organized as follows. Section 2 presents an outline of the spectral element method, including a discussion of the transport properties relevant to high-Reynolds number flow simulation. Section 3 discusses the imposition of flow division and treatment of outflow boundary conditions for turbulent flows. Section 4 briefly describes our mesh generation procedure. Section 5 presents the results of grid convergence studies for two turbulent flow cases, including experimental validation results. Section 6 closes with a brief summary.

2. Navier-Stokes Discretization

We consider numerical solution of incompressible Navier-Stokes equations in Ω ,

$$\frac{\partial \mathbf{u}}{\partial t} + \mathbf{u} \cdot \nabla \mathbf{u} = -\nabla p + \frac{1}{Re} \nabla^2 \mathbf{u}, \quad \nabla \cdot \mathbf{u} = 0, \quad (1)$$

subject to appropriate initial and boundary conditions. Here, \mathbf{u} is the velocity field, p is the pressure normalized by the density, and $Re = UD/\nu$ is the Reynolds number based on the characteristic velocity U , length scale D , and kinematic viscosity ν . For blood flow, the Newtonian assumption is valid for shear rates approximately 100 s^{-1} and above, which generally holds in larger vessels where transition is expected to take place. The use of a rigid domain follows current practice in the field, and its validity varies from vessel to vessel. For example, in arteriovenous grafts, wall motion is on the order of 1 percent of the vessel diameter [32], so a rigid assumption is a reasonable starting point for analysis of the flow transition process. Such an assumption, however, precludes incorporation of any energy storage and exchange mechanism between the flowing blood and the elastic wall. While we anticipate studying such phenomena in the near future, our focus here is on the numerical algorithms related to (1). Our discretization of (1) is based on the spectral element method (SEM) which is described in detail elsewhere (e.g., [6,9,10]). Here, we give a brief outline of the SEM and numerical timestepping scheme to provide a context for the features that are specific to the simulation of high-Reynolds number vascular flows.

For the temporal discretization, we employ a semi-implicit formulation in which the nonlinear terms are treated explicitly and the remaining linear Stokes problem is treated implicitly. The time derivative in (1) is approximated by using a k th-order backwards difference formula (BDF k , $k=2$ or 3), which for $k=2$ reads

$$\frac{3\mathbf{u}^n - 4\mathbf{u}^{n-1} + \mathbf{u}^{n-2}}{2\Delta t} = S(\mathbf{u}^n) + NL^n. \quad (2)$$

Here, \mathbf{u}^{n-q} represents the velocity at time t^{n-q} , $q = 0, \dots, 2$, and $S(\mathbf{u}^n)$ is the linear symmetric Stokes operator that implicitly incorporates the divergence-free constraint. The term NL^n approximates the nonlinear terms at time level t^n and is given by the extrapolant $NL^n := -\sum_j \alpha_j \mathbf{u}^{n-j} \cdot \nabla \mathbf{u}^{n-j}$. For $k = 2$, the standard extrapolation would use $\alpha_1 = 2$ and $\alpha_2 = -1$. Typically, however, we use a three-term second-order formulation with $\alpha_1 = 8/3$, $\alpha_2 = -7/3$, and $\alpha_3 = 2/3$, which has a stability region that encompasses a

part of the imaginary axis, similar to third-order Adams-Bashforth [20]. As an alternative to (2), we frequently use the operator-integration-factor scheme of Maday et al. [35] that circumvents the CFL (Courant-Friedrichs-Lewy) stability constraints by setting $NL^n = 0$ and replacing the left-hand side of (2) with an approximation to the material derivative of \mathbf{u} . In either case, one obtains an unsteady Stokes problem of the form

$$\begin{aligned} \mathcal{H}\mathbf{u}^n - \nabla p^n &= \mathbf{f}^n \\ \nabla \cdot \mathbf{u}^n &= 0, \end{aligned} \quad (3)$$

to be solved implicitly. For $k = 2$, \mathcal{H} is the Helmholtz operator $\mathcal{H} := (\frac{3}{2\Delta t} - \frac{1}{Re}\nabla^2)$. In Section 3, we will formally refer to (3) in operator form $S_{us}(\mathbf{u}^n) = \mathbf{f}^n$. In concluding our temporal discretization overview, we note that we often stabilize high- Re cases by filtering the velocity at each step ($\mathbf{u}^n = F(\mathbf{u}^n)$), using the high-order filter described in [10,13].

Spatial discretization of (3) is based on the $\mathbb{P}_N - \mathbb{P}_{N-2}$ spectral element method of Maday and Patera [34]. The SEM is a high-order weighted residual approach similar to the finite element method (FEM). In the SEM, functions are approximated as tensor-product Lagrange polynomials of degree N on each of E subdomains (elements), Ω^e , $e = 1, \dots, E$, leading to $n \approx EN^d$ unknown basis coefficients for each velocity component in \mathbb{R}^d , $d=1$ or 2 , with $N=4-16$ being typical. In the $\mathbb{P}_N - \mathbb{P}_{N-2}$ method, the pressure is approximated as a tensor-product polynomial of degree $N-2$ and is discontinuous, leading to $n_p = E(N-1)^d$ basis coefficients for p .

The relatively high polynomial degree of the SEM is enabled by the use of tensor-product bases having the form (in 2D)

$$\mathbf{u}(\mathbf{x}^e(r, s))|_{\Omega^e} = \sum_{i=0}^N \sum_{j=0}^N \mathbf{u}_{ij}^e h_i^N(r) h_j^N(s), \quad (4)$$

where the \mathbf{u}_{ij}^e s are the nodal basis coefficients on element Ω^e and $h_i^N \in \mathbb{P}_N$ is the Lagrange polynomial based on the Gauss-Lobatto quadrature points, $\{\xi_j^N\}_{j=0}^N$ (the zeros of $(1 - \xi^2)L'_N(\xi)$, where L_N is the Legendre polynomial of degree N). Here $\mathbf{x}^e(r, s)$ is the coordinate mapping from $\hat{\Omega} = [-1, 1]^d$ to Ω^e , implying that the elements are curvilinear quadrilaterals in 2D or hexahedra in 3D.

In the SEM, all of the operator evaluations for explicit timestepping and iterative solution of implicit substeps are performed in matrix-free form. As first suggested by Orszag [38], this approach leads to a reduction in memory and operation counts from $O(EN^6)$ (in 3D) to $O(EN^3)$ and $O(EN^4)$, respectively. Unstructured data accesses are required at the global level (i.e., for $e = 1, \dots, E$), but local data accesses within Ω^e are structured in i - j - k form. In particular, differentiation—a central kernel in operator evaluation—can be implemented as a cache-efficient matrix-matrix product. For example, $\mathbf{u}_{r,ij}^e = \sum_p \hat{D}_{ip} \mathbf{u}_{pj}^e$, with $\hat{D}_{ip} := h'_p(\xi_i)$ would return the derivative of (4) with respect to the computational coordinate r at the points (ξ_i, ξ_j) . Differentiation with respect to \mathbf{x} is obtained by the chain rule [6].

Inserting the SEM basis (4) into the weak form of (3) and applying numerical quadrature, we obtain the discrete unsteady Stokes system

$$H \underline{\mathbf{u}}^n - D^T \underline{p}^n = B \underline{\mathbf{f}}^n, \quad D \underline{\mathbf{u}}^n = 0. \quad (5)$$

Here, $H = \frac{1}{Re}A + \frac{3}{2\Delta t}B$ is the discrete equivalent of \mathcal{H} ; $-A$ is the discrete Laplacian, B is the (diagonal) mass matrix associated with the velocity mesh, D is the discrete divergence operator, and $\underline{\mathbf{f}}^n$ accounts for the explicit treatment of the nonlinear terms. Note that the Galerkin approach implies that the governing system in (5) is symmetric and that the matrices H , A , and B are all symmetric positive definite.

The Stokes system (5) is solved approximately, by using the k th-order operator splitting analyzed in [3,35,39]. The splitting is applied to the *discretized* system so that ad hoc boundary conditions are avoided. For $k = 2$, one first solves

$$H \underline{\mathbf{u}} = B \underline{\mathbf{f}}^n + D^T \underline{p}^{n-1}, \quad (6)$$

which is followed by a pressure correction step

$$E \delta \underline{p} = -D \underline{\mathbf{u}}, \quad \underline{\mathbf{u}}^n = \underline{\mathbf{u}} + \Delta t B^{-1} D^T \delta \underline{p}, \quad \underline{p}^n = \underline{p}^{n-1} + \delta \underline{p}, \quad (7)$$

where $E := \frac{2}{3} \Delta t D B^{-1} D^T$ is the Stokes Schur complement governing the pressure in the absence of the viscous term. Substeps (6) and (7) are solved with preconditioned conjugate gradient (PCG) iteration. Jacobi preconditioning is sufficient for (6) because H is strongly diagonally dominant. E is less well-conditioned and is solved either by the multilevel overlapping Schwarz method developed in [9,12] or by more recent Schwarz-multigrid methods [11,33]. The solution of (7) constitutes the most compute-intensive substep of our Navier-Stokes time advancement.

Convergence Properties

The primary distinction of the SEM is that it is designed for much higher approximation orders than are typically used with the FEM. With the SEM, orders $N=4\text{--}16$ are typical (and feasible, because of the use of matrix-free operator evaluation [6]). These high orders lead to excellent transport (minimal numerical diffusion and dispersion) for a significantly larger fraction of the resolved modes than is possible with the FEM. This point is illustrated in Fig. 1, which shows the error, ϵ_k , for eigenvalues associated with the model convection problem $u_t + u_x = 0$ on $[0, 2\pi]$ versus the fraction of resolvable modes, k/k_{\max} . Here $k_{\max} = n/2$, according to the Nyquist criterion, $n = EN$ is the number of degrees of freedom for this one-dimensional problem, and $\epsilon_k := |\tilde{k} - k|/k$. The approximate eigenvalue is computed as $\tilde{k} := (\phi'_k, D\phi_k)_N / (\phi'_k, \phi'_k)_N$, where $\phi_k(x) := \cos(kx)$, D is the spectral element derivative operator associated with E uniformly sized elements of order N , and $(\cdot, \cdot)_N$ refers to quadrature on the $N+1$ Gauss-Lobatto Legendre nodal points within each domain that also correspond to the Lagrange interpolation points. Figure 1a shows the errors for $n=512$, $N=1, 2, 4, 8, 16$, and $E := n/N$. Taking 1 percent as an acceptable error threshold (indicated by the dashed line in Fig. 1a), we see that 10 percent of the modes are well resolved with linear elements ($N=1$), whereas approximately half of the modes are well resolved for $N \geq 8$. Thus, the SEM provides roughly a fivefold reduction in the required number of gridpoints *per space dimension* to properly propagate waves at typical engineering tolerances. Note that, because the abscissa is scaled by k_{\max} , the curves in Fig. 1a exhibit little material change with increased resolution; as n increases, one resolves more waves, but the relative fraction remains unchanged. By the same token, one cannot circumvent the Nyquist sampling criterion by simply increasing N . In fact, as $N \rightarrow \infty$, one can resolve at most $(2/\pi)k_{\max}$ waves, because of the spacing of stable

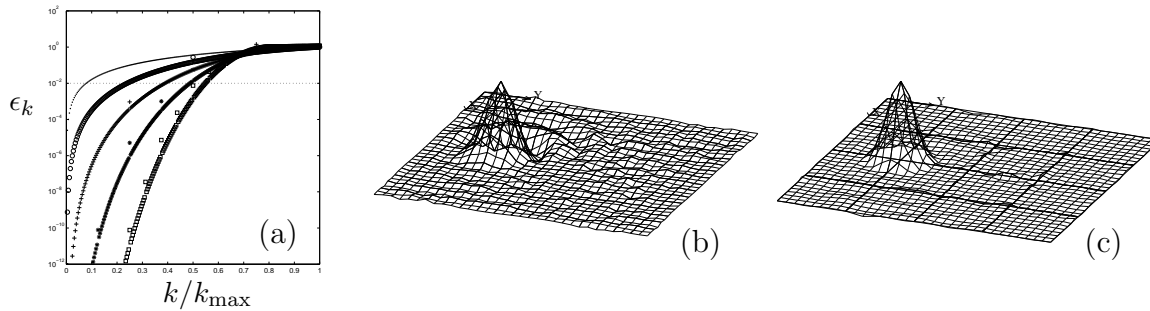


Figure 1. (a) Relative error in the 1D spectrum of $u = \lambda u_x$ versus fraction of resolvable modes for $n = 512$, $E := n/N$, and $N=1$ (\cdot), 2 (\circ), 4 ($+$), 8 ($*$), and 16 (\square); (b–c) spectral element solution of convected cone problem after a single plane-rotation on a 32×32 grid, (b) $(E, N) = (16 \times 16, 2)$, (c) $(4 \times 4, 8)$ [6].

(Gauss-type) point distributions [6]. The use of moderate values of N is motivated by the fact that one resolves nearly this number of waves with $N \approx 8$ –16.

The benefits of a minimally dispersive/dissipative spatial discretization are illustrated by the two-dimensional convection problem of Figs. 1b and c, which show the solution after an initially pointed cone is subjected to plane rotation on a pair of $n = 32 \times 32$ grids [6,18]. The second-order case, with $E = 16 \times 16$ elements, exhibits significant numerical dispersion after a single rotation. This dispersion is dramatically reduced as the order is increased to $N=8$ ($E = 4 \times 4$). The improvement is striking in light of the fact that classical theory implies that the asymptotic convergence rate for a high-order method is no better than for a low-order method if the problem is not smooth (e.g., well-resolved) [18]. In the present case, the benefits derive from the fact that the high-order case is better able to propagate those components of the solution that *are* resolved.

3. Boundary Conditions

Boundary conditions for the simulation of transition in vascular flow models present several challenges not found in classical turbulence simulations. As velocity profiles are rarely available, our usual approach at the vessel inflow is to specify a time-dependent Womersely flow that matches the first 20 Fourier harmonics of measured flow waveform. In some cases, it may be necessary to augment such clean profiles with noise in order to trigger transition at the Reynolds numbers observed in vivo. At the outflow, our standard approach is to use the natural boundary conditions (effectively, $p = 0$ and $\frac{\partial \mathbf{u}}{\partial n} = 0$) associated with the variational formulation of (3). This outflow boundary treatment is augmented in two ways for transitional vascular flows, as we now describe.

3.1. Fast Implicit Enforcement of Flow Division

Imposition of proper flow division (or flow split) is central to accurate simulation of vascular flows through bifurcations (sites prone to atherogenesis). The distribution of volumetric flow rate through multiple daughter branches is usually available through measured volume flow rates. A typical distribution in a carotid artery bifurcation, for

example, is a 60:40 split between the internal and external carotid arteries. The distribution can be time-dependent, and the method we outline below is applicable to such cases. A common approach to imposing a prescribed flow split is to apply Dirichlet velocity conditions at one outlet and standard outflow (Neumann) conditions at the other. The Dirichlet branch is typically artificially extended to diminish the influence of spurious boundary effects on the upstream region of interest. Here, we present an approach to imposing arbitrary flow divisions among multiple branches that allows one to use Neumann conditions at each of the branches, thus reducing the need for extraordinary extensions of the daughter branches.

Our flow-split scheme exploits the semi-implicit approach outlined in the preceding section. The key observation is that the unsteady Stokes operator, which is treated implicitly and which controls the boundary conditions, is *linear* and that superposition therefore applies. Thus, if $\tilde{\mathbf{u}}^n$ satisfies $S_{us}(\tilde{\mathbf{u}}^n) = \mathbf{f}^n$ and $\tilde{\mathbf{u}}_0$ satisfies $S_{us}(\tilde{\mathbf{u}}_0) = 0$ but with different boundary conditions, then $\mathbf{u}^n := \tilde{\mathbf{u}}^n + \tilde{\mathbf{u}}_0$ will satisfy $S_{us}(\mathbf{u}^n + \tilde{\mathbf{u}}_0) = \mathbf{f}^n$ with boundary conditions $\mathbf{u}^n|_{\partial\Omega} = \tilde{\mathbf{u}}^n|_{\partial\Omega} + \tilde{\mathbf{u}}_0|_{\partial\Omega}$. With this principle, the flow split for a simple bifurcation (one common inflow, two daughter outflow branches) is imposed as follows. In a preprocessing step:

- (i) Solve $S_{us}(\tilde{\mathbf{u}}_0) = 0$ with a prescribed inlet profile having flux $\tilde{Q} := \int_{\text{inlet}} \tilde{\mathbf{u}}_0 \cdot \mathbf{n} dA$, and no flow (i.e., homogeneous Dirichlet conditions) at the exit of one of the daughter branches. Use Neumann (natural) boundary conditions at the the other branch. Save the resultant velocity-pressure pair $(\tilde{\mathbf{u}}_0, \tilde{p}_0)$.
- (ii) Repeat the above procedure with the role of the daughter branches reversed, and call the solution $(\tilde{\mathbf{u}}_1, \tilde{p}_1)$.

Then, at each timestep:

- (iii) Compute $(\tilde{\mathbf{u}}^n, \tilde{p}^n)$ satisfying (3) with homogeneous Neumann conditions on each daughter branch, and compute the associated fluxes $\tilde{Q}_i^n := \int_{\partial\Omega_i} \tilde{\mathbf{u}}^n \cdot \mathbf{n} dA$, $i=0, 1$, where $\partial\Omega_0$ and $\partial\Omega_1$ are the respective active exits in (i) and (ii).
- (iv) Solve the following for (α_0, α_1) to obtain the desired flow split $Q_0^n:Q_1^n$:

$$Q_0^n = \tilde{Q}_0^n + \alpha_0 \tilde{Q} \quad (\text{desired flux on branch 0}) \quad (8)$$

$$Q_1^n = \tilde{Q}_1^n + \alpha_1 \tilde{Q} \quad (\text{desired flux on branch 1}) \quad (9)$$

$$0 = \alpha_0 + \alpha_1 \quad (\text{change in flux at inlet}) \quad (10)$$

- (v) Correct the solution by setting $\mathbf{u}^n := \tilde{\mathbf{u}}^n + \sum_i \alpha_i \tilde{\mathbf{u}}_i$ and $p^n := \tilde{p}^n + \sum_i \alpha_i \tilde{p}_i$.

Remarks. The above procedure provides a fully implicit iteration-free approach to applying the flow split that readily extends to a larger number of branches by expanding the system (8)–(10). Condition (10) ensures that the net flux at the inlet is unchanged and, for a simple bifurcation, one needs only to store the difference between the auxiliary solutions. We note that S_{us} is dependent on the timestep size Δt and that the auxiliary solutions $(\tilde{\mathbf{u}}_i, \tilde{p}_i)$ must be recomputed if Δt (or ν) changes. (One must also recompute

the auxiliary solutions if the geometry changes, as would be the case when computing fluid-structure interaction. In such situations, the iterative approach of Gin et al. might be more appropriate [16].) The amount of viscous diffusion that can take place in a single application of the unsteady Stokes operator is governed by Δt , and one finds that the auxiliary solutions have relatively thin boundary layers with a broad flat core. The intermediate solutions obtained in (iii) have inertia and so nearly retain the proper flow split, once established, such that the magnitude of α_i will be relatively small after just a few timesteps. It is usually a good idea to gradually ramp up application of the correction if the initial condition is not near the desired flow split. Otherwise, one runs the risk of having reversed flow on portions of the outflow boundary and subsequent instability, as discussed in the next section. Moreover, to accommodate the exit “nozzle” ($\nabla \cdot \mathbf{u} > 0$) condition introduced below, which changes the net flux out of the exit, we compute \tilde{Q}_i^n at an upstream cross-section where $\nabla \cdot \mathbf{u} = 0$.

3.2. Turbulent Outflow Boundary Conditions

Turbulent flows can generate vortices of sufficient strength to create a (locally) negative flux at the outflow boundary. Because the Neumann boundary condition does not specify flow characteristics at the exit, a negative flux at the outflow can rapidly lead to instability, with catastrophic results. One way to eliminate incoming characteristics is to force the exit flow through a nozzle, effectively adding a mean axial component to the velocity field. The advantage of using a nozzle is that one can ensure that the characteristics at the exit point outward under a wide range of flow conditions. By contrast, schemes based on viscous buffer zones require knowledge of the anticipated space and time scales to ensure that vortical structures are adequately damped as they pass through the buffer zone.

Numerically, a nozzle can be imposed without change to the mesh geometry by imparting a positive divergence to the flow field near the exit (in the spirit of a supersonic nozzle). In our simulations, we identify the layer of elements adjacent to the outflow and there impose a divergence $D(\mathbf{x})$ that ramps from zero at the upstream end of the layer to a fixed positive value at the exit. Specifically, we set $D(\mathbf{x}) = C[1 - (x_\perp/L_\perp)^2]$, where x_\perp is the distance normal to the boundary and L_\perp is maximum thickness of the last layer of elements. By integrating the expression for D from $x_\perp/L_\perp = 1$ to 0, one obtains the

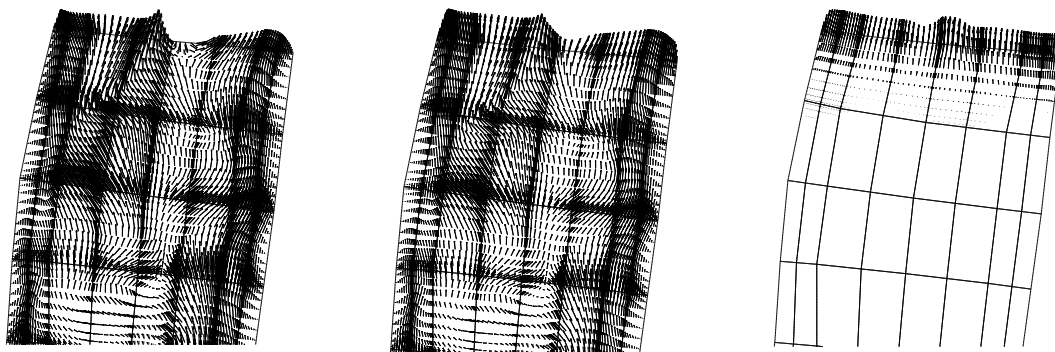


Figure 2. Velocity vectors near the outflow of an internal carotid artery: (left) uncorrected, (center) corrected, and (right) corrected minus uncorrected.

net gain in mean velocity over the extent of the layer. We typically choose the constant C such that the gain is equal to the mean velocity prior to the correction. One could, however, increase the gain if stronger fluctuations are encountered.

Results for the nozzle-based outflow condition are illustrated in Fig. 2. The left panel shows the velocity field for the standard (uncorrected Neumann) condition near the outflow boundary of an internal carotid artery at $Re \approx 1400$ (based on the peak flow rate and stenosis diameter). Inward-pointing velocity vectors can be seen at the exit boundary, and the simulation becomes catastrophically unstable within 100 timesteps beyond this point. The center panel shows the flow field computed with the outflow correction. The flow is leaving the domain at all points along the outflow boundary and the simulation is stable for all time. The difference between the two cases (right) shows that the outflow treatment does not pollute the solution upstream of the boundary.

4. Mesh Generation

Spectral element mesh generation shares much in common with its FE counterpart. Several important distinctions, however, place constraints on the SE meshes. First, the use of matrix-free operator evaluation, which reduces the storage from $O(EN^6)$ to $O(EN^3)$ and work per evaluation from $O(EN^6)$ to $O(EN^4)$, is dependent upon the tensor-product forms (4). This reduction is most effectively achieved with hexahedral elements, which may be curved through the use of iso- or subparametric mappings from $\hat{\Omega}$ to Ω^e [6]. Second, the fact that typical orders are in the range $N=8$ to 16 implies roughly a thousandfold reduction in the number of elements required compared to an FE mesh at comparable resolution. The reduction, while advantageous in reducing the size of the input files, places significant constraints on the mesh generation scheme. Consequently, we have developed an SE mesh generation scheme that is specific to vascular geometries [27,43].

Our mesh generation scheme employs a sweeping algorithm, in which disc-shaped slabs are meshed by using a standard O-grid configuration, as illustrated in Fig. 3. The slab surfaces are identified with isosurfaces of conduction (potential) solutions satisfying homogeneous Neumann conditions along the vessel wall. The isosurfaces are computed by numerically solving a sequence of Laplace equations, one for each branch, in the computational domain on a preliminary mesh comprising tetrahedral elements. Because of the robustness of the conduction problem, the preliminary mesh can be of almost arbitrary quality. The isosurfaces define a set of natural coordinate systems that have the desirable properties of being orthogonal to the vessel walls and of being guaranteed to produce nonintersecting cross-sections that could otherwise lead to vanishing Jacobians associated with the transformation from $\hat{\Omega}$ to Ω^e . Through a judicious choice of conduction problems, one can identify three principal isosurfaces that naturally trisect the bifurcation geometry, as depicted in Fig. 3b. This trisection leads to a decomposition of the bifurcation into three branches, each of which is individually meshed with the sweeping algorithm. The advantages of the conduction-based approach is that it can be automated (starting with a segmented stack, mesh generation requires a matter of minutes on a workstation [43]) and it produces high-quality all-hexahedral meshes with a minimum number of topology-induced defects.

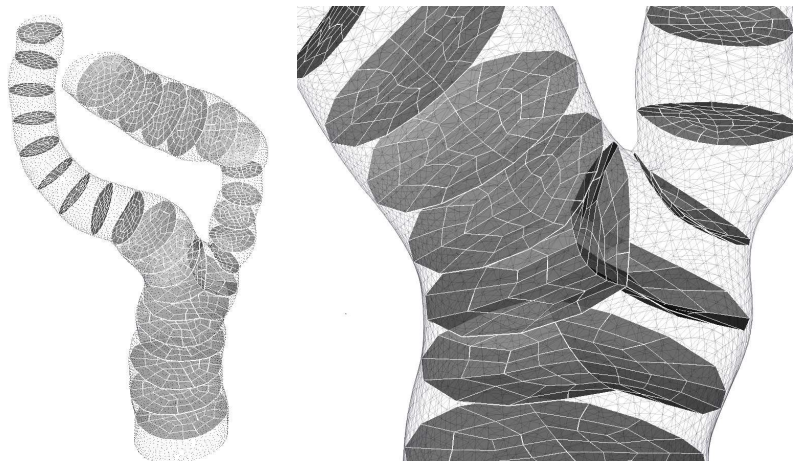


Figure 3. Swept templates, projected onto isopotential surfaces, for hexahedral mesh generation in a carotid bifurcation geometry. The closeup on the right shows the principal isosurfaces from the three conduction problems that provide a uniquely determined trisection of the domain into independently swept branches [43].

5. Resolution Requirements

An important component of any numerical study is the establishment of adequate resolution. This is particularly challenging in turbulent flows because one can expect to converge only in the mean and higher-order statistics, which require long-time simulations to eliminate natural fluctuations as a source of variance. For pulsatile turbulent flows, it is necessary to use phase averaging, in which one samples the solution at a certain phase of the cardiac cycle over a large number of cycles and then averages these results. Experiments in the transitional flow regime have shown that relatively slow pulsatility coupled to rapidly evolving turbulence merely acts as a switch that turns the turbulence on or off and does not materially change the turbulent state [24,1]. Thus, given the length of the cardiac cycle (>10 flow-through times for a typical bifurcation model) and the number of samples required to reach a statistically stationary state, it is preferable to test for grid convergence by simply using steady inlet conditions at the peak Reynolds numbers. One can then exploit temporal homogeneity and ergodicity to obtain mean and rms velocity distributions that can be used for convergence tests.

As with its global spectral counterpart, the standard convergence procedure for the spectral element method is to increase the polynomial degree N for a fixed number of elements E . It is also possible, however, to use an adaptive procedure in which one refines the mesh and varies the polynomial degree locally to obtain optimal convergence rates, as is done with hp finite element methods [21,36]. Our general approach has been to construct a mesh that is finest in the region of interest, starting with relatively low degree (typ., $N=4$), and to then increase N as we increase the Reynolds number. We typically construct the mesh such that, at the target Reynolds number, $N=8-12$ will be sufficient. This range of N is typically optimal for the performance of our spectral element code

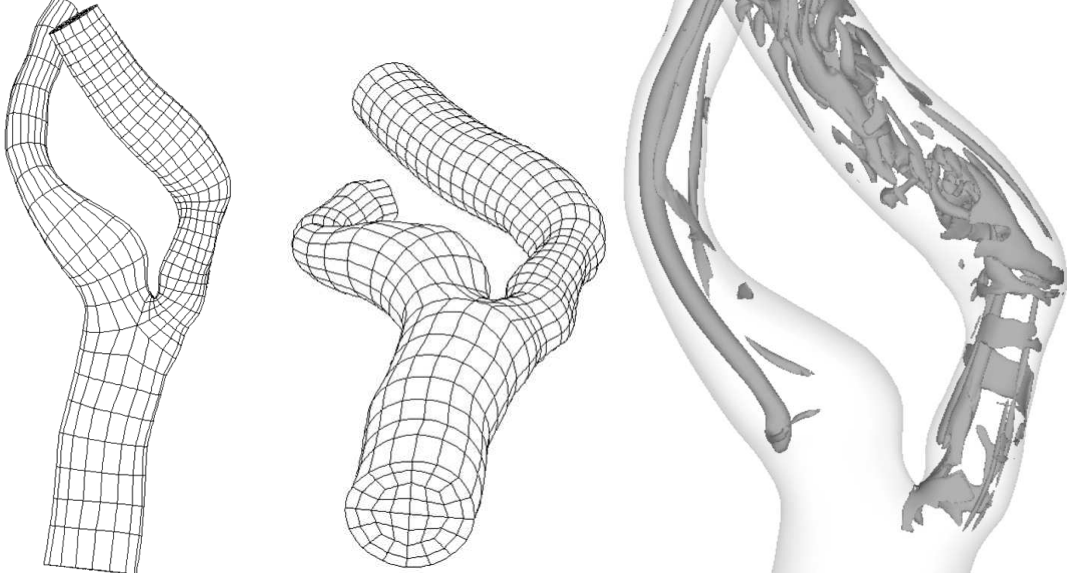


Figure 4. (a) and (b) $E=2544$ element mesh for stenosed carotid artery simulations and (c) coherent vortical structures at systolic mid-deceleration phase identified by using the λ_2 criterion of Jeong and Hussain [23].

and, as illustrated in Fig. 1, provides a significant fraction of the maximal benefit to be derived from high-order approximations.

In this section, we examine the resolution requirements for direct numerical simulation of turbulence in two cases, flow in a stenosed carotid artery and flow in an arteriovenous graft. As a measure of convergence, we present time-averaged and rms velocity distributions as a function of resolution (N) for a fixed number of elements. We note that convergence of these profiles is really a minimal requirement for spatial convergence. For example, Ethier et al. [7] have pointed out that accurate determination of wall shear stress or wall shear stress gradient distributions represent even more stringent convergence criteria, even in the case of laminar flows.

5.1. Stenosed Carotid Artery Flow

Atherothrombotic carotid stenoses, followed by ischemic stroke, is one of the leading causes of mortality and morbidity in Western countries [37]. The presence of high-grade stenosis manifested by plaque deposits can result in transition to turbulent flow, which may produce an audible sound (bruit) discernible by a physician.

Many studies have been conducted to characterize local hemodynamics and their role on the early development of atherosclerosis in arteries. Atherosclerotic-prone sites are often localized at bifurcations, junctions, and regions of high curvature, which are also regions of low wall shear stress (WSS) and flow disruption [2,4,17,26,45].

In contrast, regions downstream of severe constrictions (post-stenotic regions) experience a significantly different biomechanical environment than do healthy vessels because of the presence of transitional and turbulent flow. Because flow resistance is primarily

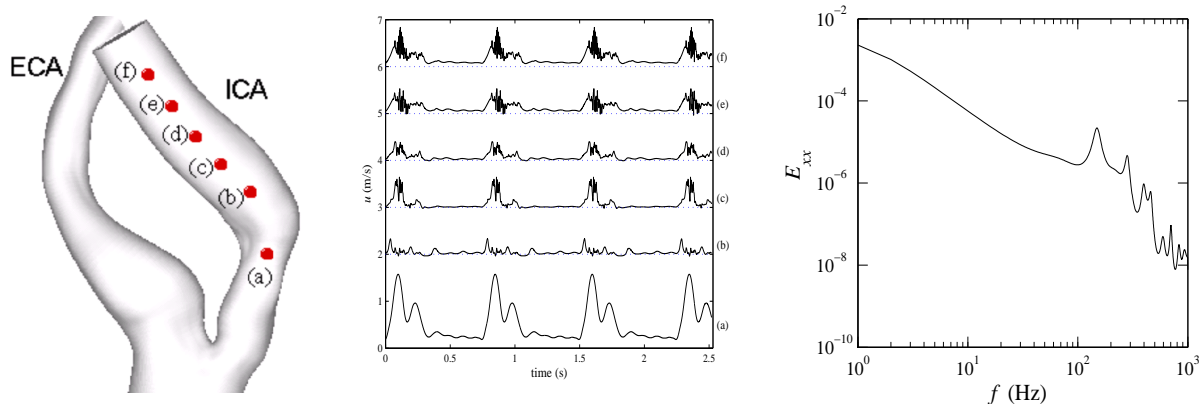


Figure 5. Pulsatile velocity results for a stenosed carotid artery: (a) time history points, (b) time traces of axially aligned velocity for four cardiac cycles, and (c) axial velocity energy spectra for point (f).

controlled by smaller vessels downstream (arterioles and capillaries), the presence of a stenosis does not materially change the flow rate. The area reduction within a stenosis thus accelerates the flow and leads to high WSS. This high WSS and the presence of turbulence may damage the endothelial cells [14,19] and play a role in platelet activation [41] or plaque rupture [15]. In addition, the large spatial WSS gradient associated with turbulent flow is thought to enhance mass transport into the arterial wall proximal to the stenosis, which may weaken the plaque and make it vulnerable to rupture [5]. High temporal shear gradients are also shown to stimulate endothelial cell proliferation [44]. The ability to accurately predict the hemodynamics in such an environment is of interest to clinicians and researchers alike.

We have undertaken a numerical study of pulsatile flow in a carotid bifurcation model that exhibits a severe stenosis ($\sim 75\%$ area reduction) in the internal carotid artery (ICA) [28]. The computational mesh, shown in Fig. 4a and b, comprises $E=2544$ spectral elements generated by using the potential-based approach described in Section 4. A time-dependent Womersley profile, synthesized from phase averages of measured flow waveforms, was imposed at the inlet to the common carotid artery (CCA), and a 40:60 split was imposed between the external (ECA) and internal (ICA) branches throughout the 0.75 sec cardiac cycle by using the technique described in Section 3. The Reynolds number, based on the ICA diameter and bulk velocity, ranged from 380 at diastole to 1320 at peak systole. For $N=9$, a timestep of $\Delta t = 5 \times 10^{-6}$ sec (150,000 steps/cycle) guaranteed a Courant-Freidrichs-Lewy (CFL) number of < 0.5 throughout the cycle, which ensured stability of the semi-implicit time advancement. Each cardiac cycle required 20 hours of CPU time on 256 processors of the TCS1 parallel computer at the Pittsburgh Supercomputer Center.

Although our primary focus is on the resolution requirements for turbulent vascular flows, we present some flow details here in order to indicate where resolution is required. (A more detailed description of this set of simulations is provided in [28].) Figure 4c shows a set of typical vortical structures, identified by the λ_2 criterion of Jeong and Hussein [23],

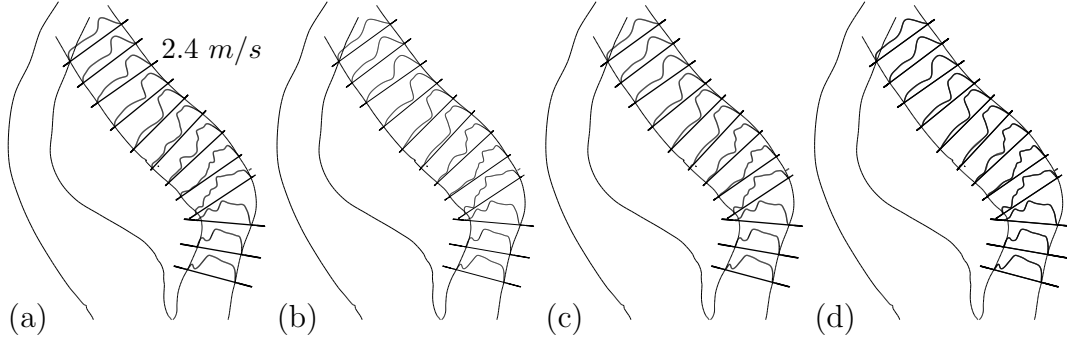


Figure 6. Comparison of time-averaged velocity profiles for transitional flow under steady inlet conditions: (a) $N=7$, (b) $N=9$, (c) $N=11$, (d) $N=9$ and 11 overlaid.

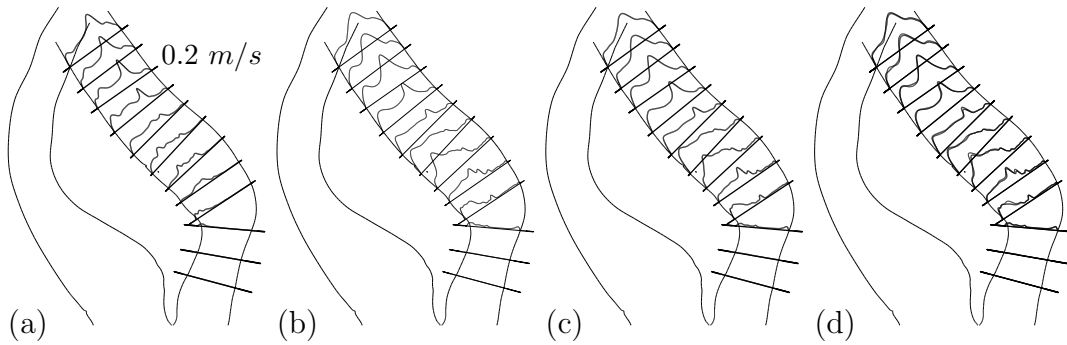


Figure 7. Comparison of rms profiles of axial velocity for transitional flow under steady inlet conditions: (a) $N=7$, (b) $N=9$, (c) $N=11$, (d) $N=9$ and 11 overlaid.

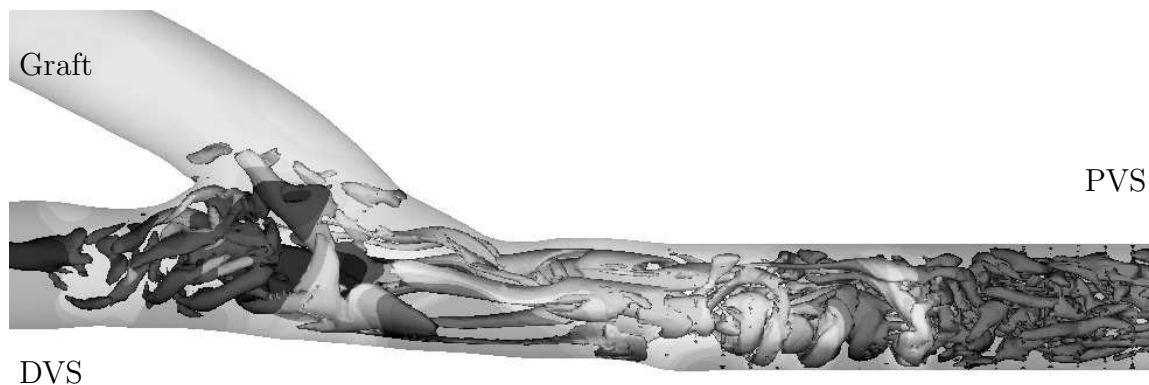


Figure 8. Coherent structures in an AV graft at $Re = 1200$ with a 70:30 (PVS:DVS) flow split. The simulation employed $E=2640$ elements of order $N = 12$ and $\Delta t = 5 \times 10^6 s$ (from [31]).

in the mid-deceleration phase past peak systole. The presence of transverse rolls, stretched by the mean shear, and the increase in small-scale structure downstream of the stenosis are hallmarks of the transition process. Nearer to the systolic peak (not shown) the flow is significantly more complex, with less clearly identifiable structure. The ICA is to be contrasted with the ECA, where the flow exhibits one or two dominant axial vortices that do not break down—the flow in the ECA remains laminar. Further evidence of the spatio-temporal resolution requirements is given in Fig. 5b, which shows time traces of axial velocity at points (a)–(f), indicated in Fig. 5a. The passage of small-scale structures registers as high-frequency variation in velocities in the post-stenotic region. A Fourier transform of the time trace for (f), shown in Fig. 5c, reveals significant spectral peaks in the range ~ 150 – 500 Hz, which is much higher than the order-unity frequencies associated with the cardiac cycle.

To address the question of resolution, we have undertaken a series of runs with *steady* inlet conditions at a flow rate corresponding to that just beyond the systolic peak, where maximum turbulence intensity is observed in the pulsatile case. Simulations with $N = 7$, 9, and 11 ($n = 850000$, 1820000, and 3338000 points, respectively) were run from the same turbulent initial condition for 33 flow-through times, with statistics collected over the last 30 flow-through times. The average and rms velocity profiles in the ICA mid-plane are shown in Figs. 6 and 7, respectively. The results show that $N=9$ and 11 give nearly identical mean and rms distributions, whereas $N=7$ shows significant deficiencies, particularly for the rms. This study indicates that approximately 2 million gridpoints are required to adequately resolve this flow when 9th-order spectral elements are used.

5.2. Transition in an Arteriovenous Graft

Arteriovenous (AV) grafts consist of a ~ 15 cm section of 6 mm i.d. synthetic tubing that is surgically implanted to provide an arterial-to-vein round-the-clock short circuit. Because they connect a high-pressure vessel to a low-pressure one, high flow rates are established that make AV grafts efficient dialysis ports for patients suffering from poor kidney function. The high-speed flow is normally accompanied by transition to a weakly

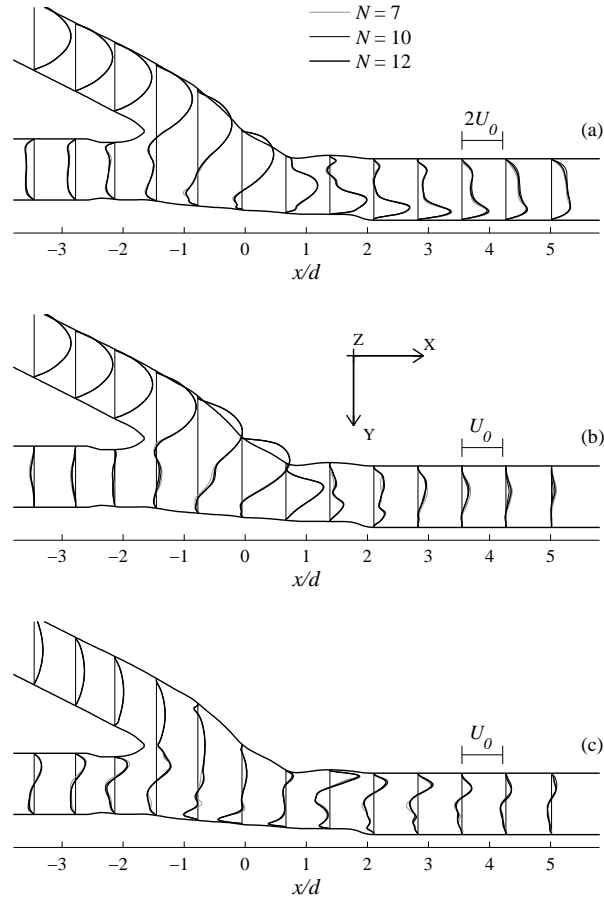


Figure 9. Comparison of time-averaged velocity profiles in the AV graft for transitional flow under steady inlet conditions with a 70:30 (PVS:DVS) flow split: (a) u , (b) v , and (c) w .

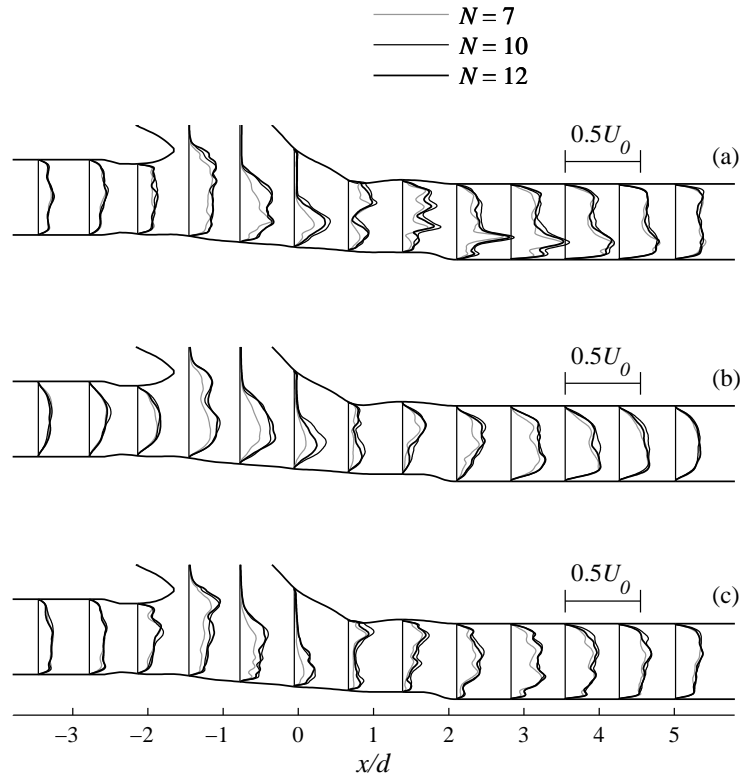


Figure 10. Comparison of rms velocity profiles in the AV graft for transitional flow under steady inlet conditions with a 70:30 (PVS:DVS) flow split: (a) u_{rms} , (b) v_{rms} , and (c) w_{rms} .

turbulent state, manifested as a 200–300 Hz vibration at the vein wall [29,32]. This high-frequency excitation is thought to lead to intimal hyperplasia, which can lead to complete occlusion of the vein and graft failure within six months of implant. We are investigating the mechanisms leading to transition in subject-specific AV-graft models with the aim of reducing turbulence through improved geometries. Detailed comparisons with laser Doppler anemometry (LDA) measurements are presented in [31]. Results for a pulsatile flow study are given in [29], and the influence of the flow division between the proximal venous segment (PVS) and distal venous segment (DVS) is discussed in [30].

Figure 8 shows a typical turbulent case when there is a 70:30 split between the PVS and DVS. Significant small-scale structures are generated downstream (toward the heart) of the anastomosis in the PVS, which channels the majority of the flow. Steady graft inlet conditions are imposed, with a mean (cross-sectional average) velocity of U_0 . The Reynolds number based on the graft diameter is $Re := U_0 D / \nu = 1200$. The SEM solution was computed with $E=2640$ elements of order 12 (4.5 million gridpoints).

A grid independence study was performed at Reynolds number 1200 with a flow split of 70:30, corresponding to the conditions shown in Fig. 8. Comparisons of time-averaged velocity and root-mean-square (rms) of the velocity fluctuation with $N = 7, 10$, and 12 for the 70:30 flow division are shown in Figs. 9 and 10, respectively. Statistics were gathered for 1 second after an initial transient of 0.15 seconds, which was not included in the statistics. (For comparison, the mean flow-through time is ~ 0.1 seconds in vivo units; $D=6$ mm and $U_0 = 649$ mm/sec). The time-averaged velocity did not show significant change for $N=7, 10$ or 12 . However, the rms of velocity showed noticeable change between polynomial orders, even in the results of $N = 12$. This dependency could be attributed to statistical variance over the collection period or indicate the need for still higher grid resolution. However, the results with $N = 12$ are adequate for demonstrating the primary features of the flow since the rms of velocity is observed to be bounded in Fig. 10 with increasing polynomial order.

Based on these grid independence studies, the numerical results with $N = 12$ were used for validation with experimental measurements obtained using laser Doppler anemometry (LDA), as described in [31]. Figure 11 shows a comparison of mean and rms cross-sectional velocity distributions in the turbulent PVS flow with a 70:30 flow split at $Re=1200$. Measurements were taken at stations $x/D=1.34, 2.34$, and 3.34 (see Fig. 9). It is clear that the $N=12$ case is able to accurately predict both the mean flow distribution and the rms fluctuations.

6. Summary

We have presented methodology and convergence results for the application of a high-order spectral element method to the simulation of vascular flows. We have demonstrated a fast implicit approach to imposition of arbitrary flow division among daughter branches that avoids the need for extraordinary extensions or iteration to determine exit pressures. We have also developed an outflow treatment for turbulent flows that eliminates incoming characteristics that can destabilize the simulation. We have demonstrated some of the desirable transport properties of high-order discretizations that are relevant to turbulent flows and shown that roughly 2–4 million points are required for direct numerical simula-

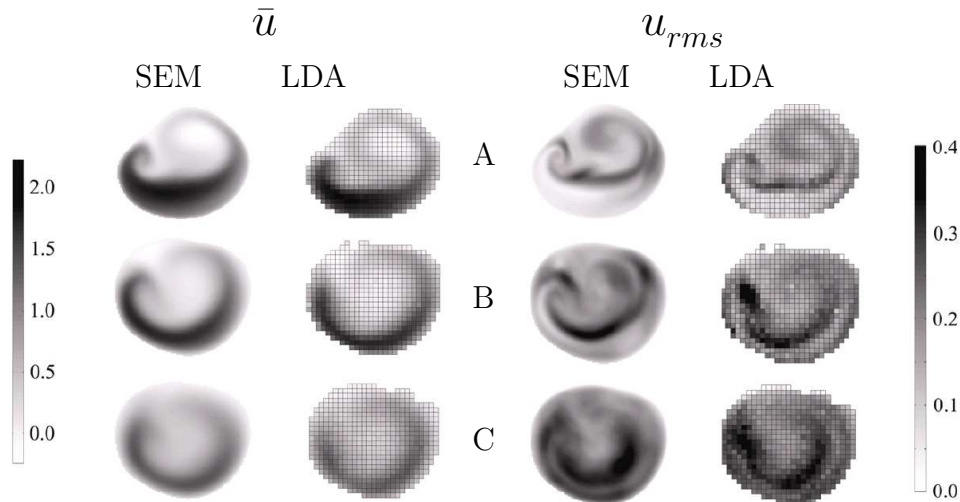


Figure 11. Numerical (SEM) / experimental (LDA) validation for AV graft flow with a 70:30 flow split and $Re=1200$: cross-sectional mean and rms velocity distributions (m/sec) at $x/D = 1.34$ (A), 2.34 (B), and 3.34 (C). (See Fig. 9.)

tion of turbulent vascular flows in bifurcation geometries at clinically relevant Reynolds numbers. These results have been validated through detailed comparisons with LDA measurements.

Acknowledgments

This work was supported by the National Institutes of Health, RO1 Research Project Grant (2RO1HL55296-04A2), by Whitaker Foundation Grant (RG-01-0198), and by the Mathematical, Information, and Computational Sciences Division subprogram of the Office of Advanced Scientific Computing Research, U.S. Department of Energy, under Contract W-31-109-Eng-38.

REFERENCES

1. N. Arslan, *Experimental characterization of transitional unsteady flow inside a graft-to-vein junction*, Ph.D. thesis, University of Illinois, Chicago, 1999, Dept. of Mech. Eng.
2. C. G. Caro, J. M. Fitz-Gerald, and R. C. Schroter, *Arterial wall shear and distribution of early atheroma in man*, *Nature* **223** (1969), no. 211, 1159–60.
3. W. Couzy, *Spectral element discretization of the unsteady Navier-Stokes equations and its iterative solution on parallel computers*, Ph.D. thesis, Swiss Federal Institute of Technology-Lausanne, 1995, Thesis nr. 1380.
4. M. J. Davies, N. Woolf, P. M. Rowles, and J. Pepper, *Morphology of the endothelium over atherosclerotic plaques in human coronary arteries*, *British Heart Journal* **60** (1988), no. 6, 459–64.

5. N. DePaola, M.A. Gimbrone, P.F. Davies, and C.F. Dewey, *Vascular endothelium responds to fluid shear stress gradients*, *Arteriosclerosis Thrombosis* **12** (1992), no. 11, 1254–7.
6. M.O. Deville, P.F. Fischer, and E.H. Mund, *High-order methods for incompressible fluid flow*, Cambridge University Press, Cambridge, 2002.
7. C.R. Ethier, S. Prakash, D.A. Steinman, R.L. Leask, G.G. Couch, and M. Ojha, *Steady flow separation patterns in a 45 degree junction*, *J. Fluid Mech.* **411** (2000), 1–38.
8. M. F. Fillinger, E. R. Reinitz, R. A. Schwartz, D. E. Resetarits, A. M. Paskanik, and C. E. Bredenberg, *Beneficial effects of banding on venous intimal-medial hyperplasia in arteriovenous loop grafts*, *J. Vasc. Surg.* **11** (1990), no. 4, 556–66.
9. P.F. Fischer, *An overlapping Schwarz method for spectral element solution of the incompressible Navier-Stokes equations*, *J. Comput. Phys.* **133** (1997), 84–101.
10. P.F. Fischer, G.W. Kruse, and F. Loth, *Spectral element methods for transitional flows in complex geometries*, *J. Sci. Comput.* **17** (2002), 81–98.
11. P.F. Fischer and J.W. Lottes, *Hybrid Schwarz-multigrid methods for the spectral element method: Extensions to Navier-Stokes*, Domain Decomposition Methods in Science and Engineering Series (R. Kornhuber, R. Hoppe, J. Piaux, O. Pironneau, O. Widlund, and J. Xu, eds.), Springer, Berlin, 2004.
12. P.F. Fischer, N.I. Miller, and H.M. Tufo, *An overlapping Schwarz method for spectral element simulation of three-dimensional incompressible flows*, *Parallel Solution of Partial Differential Equations (Berlin)* (P. Bjørstad and M. Luskin, eds.), Springer, 2000, pp. 158–180.
13. P.F. Fischer and J.S. Mullen, *Filter-based stabilization of spectral element methods*, *Comptes rendus de l'Académie des sciences, Série I- Analyse numérique* **332** (2001), 265–270.
14. D. L. Fry, *Acute vascular endothelial changes associated with increased blood velocity gradients*, *Circulation Research* **22** (1968), no. 2, 165–97.
15. S. D. Gertz and W. C. Roberts, *Hemodynamic shear force in rupture of coronary arterial atherosclerotic plaques*, *American Journal of Cardiology* **66** (1990), no. 19, 1368–72.
16. R. Gin, A.G. Straatman, and D.A. Steinman, *A dual-pressure boundary condition for use in simulations of bifurcating conduits*, *J. Biomech. Eng.* **124** (2002), 617–619.
17. S. Glagov, C. K. Zarins, D.P. Giddens, and D.N. . Ku, *Hemodynamics and atherosclerosis. insights and perspectives gained from studies of human arteries*, *Archives of Pathology and Laboratory Medicine* **112** (1988), 1018–1031.
18. D. Gottlieb and S.A. Orszag, *Numerical analysis of spectral methods: Theory and applications*, SIAM-CBMS, Philadelphia, 1977.
19. J. D. Hellums, *The resistance to oxygen transport in the capillaries relative to that in the surrounding tissue*, *Microvascular Research* **13** (1977), no. 1, 131–6.
20. L.W. Ho, *A Legendre spectral element method for simulation of incompressible unsteady viscous free-surface flows*, Ph.D. thesis, Massachusetts Institute of Technology, 1989, Cambridge, MA.
21. L.C. Hsu and C. Mavriplis, *Adaptive meshes for the spectral element method*, Domain Decomposition 9 Proc. (New York) (P. Bjørstad, M. Espedal, and D. Keyes, eds.), J.

- Wiley, 1997, pp. 374–381.
22. KJ Hutchison and E Karpinski, *In vivo demonstration of flow recirculation and turbulence downstream stenoses in canine arteries*, J. Biomech. **18** (1985), 285–296.
 23. J. Jeong and F. Hussain, *On the identification of a vortex*, J. Fluid Mech. **285** (1995), 69–94.
 24. P.S. Klebanoff, W.G. Cleveland, and K.D. Tidstrom, *On the evolution of a turbulent boundary layer induced by a three-dimensional roughness element*, J. Fluid Mech. **92** (1992), 101–187.
 25. D. N. Ku, *Blood flow in arteries*, Annu. Rev. Fluid Mech. **29** (1997), 399–434.
 26. D. N. Ku, D. P. Giddens, C. K. Zarins, and S. Glagov, *Pulsatile flow and atherosclerosis in the human carotid bifurcation*, Arteriosclerosis **5** (1985), no. 3, 293–302.
 27. S.E. Lee, *Solution method for transitional flow in a vascular bifurcation based on in vivo medical images*, Master’s thesis, Univ. of Illinois, Chicago, 2002, Dept. of Mechanical Engineering.
 28. S.E. Lee, S-W Lee, P.F. Fischer, H.S. Bassiouny, and F. Loth, *Direct numerical simulation of transitional flow in a stenosed carotid bifurcation*, J. Biomech. (submitted).
 29. S.W. Lee, P.F. Fischer, F. Loth, T.J. Royston, J.K. Grogan, and H.S. Bassiouny, *Flow-induced vein-wall vibration in an arteriovenous graft*, J. of Fluids and Structures **20** (2005), 837–852.
 30. S.W. Lee, D.S. Smith, F. Loth, P.F. Fischer, and H.S. Bassiouny, *Importance of flow division on transition to turbulence within an arteriovenous graft*, J. Biomechanics **in press** (2006).
 31. ———, *Numerical and experimental simulation of transitional flow in a blood vessel junction*, Num. Heat Transfer **in press** (2006).
 32. F. Loth, N. Arslan, P. F. Fischer, C. D. Bertram, S. E. Lee, T. J. Royston, R. H. Song, W. E. Shaalan, and H. S. Bassiouny, *Transitional flow at the venous anastomosis of an arteriovenous graft: Potential relationship with activation of the ERK1/2 mechanotransduction pathway*, ASME J. Biomech. Engr. **125** (2003), 49–61.
 33. J. W. Lottes and P. F. Fischer, *Hybrid multigrid/Schwarz algorithms for the spectral element method*, J. Sci. Comput. **24** (2005), 45–78.
 34. Y. Maday and A.T. Patera, *Spectral element methods for the Navier-Stokes equations*, State-of-the-Art Surveys in Computational Mechanics (A.K. Noor and J.T. Oden, eds.), ASME, New York, 1989, pp. 71–143.
 35. Y. Maday, A.T. Patera, and E.M. Rønquist, *An operator-integration-factor splitting method for time-dependent problems: Application to incompressible fluid flow*, J. Sci. Comput. **5** (1990), 263–292.
 36. C. Mavriplis, *Adaptive mesh strategies for the spectral element method*, Comput. Methods Appl. Mech. Engrg. **116** (1994), 77–86.
 37. C. J. Murray and A. D. Lopez, *Alternative projections of mortality and disability by cause 1990-2020: Global burden of disease study*, Lancet **349** (1997), no. 9064, 1498–504.
 38. S.A. Orszag, *Spectral methods for problems in complex geometry*, J. Comput. Phys. **37** (1980), 70–92.
 39. J.B. Perot, *An analysis of the fractional step method*, J. Comp. Phys. **108** (1993), 51–58.

40. S. J. Ram, A. Magnasco, S. A. Jones, A. Barz, L. Zsom, S. Swamy, and W. D. Paulson, *In vivo validation of glucose pump test for measurement of hemodialysis access flow*, Am J Kidney Dis **42** (2003), no. 4, 752–60.
41. J. M. Ramstack, L. Zuckerman, and L. F. Mockros, *Shear-induced activation of platelets*, Journal of Biomechanics **12** (1979), no. 2, 113–25.
42. S.J. Sherwin and H.M. Blackburn, *Three-dimensional instabilities and transition of steady and pulsatile axisymmetric stenotic flows*, J. Fluid Mech. **533** (2005), 297–327.
43. C.S. Verma, P.F. Fischer, S.E. Lee, and F. Loth, *An all-hex meshing strategy for bifurcation geometries in vascular flow simulation*, Proc. of the 14th Int. Meshing Roundtable, San Diego, 2005.
44. C. R. White, M. Haidekker, X. Bao, and J. A. Frangos, *Temporal gradients in shear, but not spatial gradients, stimulate endothelial cell proliferation*, Circulation **103** (2001), no. 20, 2508–13.
45. C. K. Zarins, D. P. Giddens, B. K. Bharadvaj, V. S. Sottiurai, R. F. Mabon, and S. Glagov, *Carotid bifurcation atherosclerosis. quantitative correlation of plaque localization with flow velocity profiles and wall shear stress*, Circulation Research **53** (1983), no. 4, 502–14.

The submitted manuscript has been created by the University of Chicago as Operator of Argonne National Laboratory ("Argonne") under Contract No. W-31-109-ENG-38 with the U.S. Department of Energy. The U.S. Government retains for itself, and others acting on its behalf, a paid-up, nonexclusive, irrevocable worldwide license in said article to reproduce, prepare derivative works, distribute copies to the public, and perform publicly and display publicly, by or on behalf of the Government.